

# E-Glass/DGEBA/*m*-PDA Single Fiber Composites: Interface Debonding During Fiber Fracture

G.A. Holmes, R.C. Peterson, D.L. Hunston, W.G. McDonough

Polymers Division, National Institute of Standards and Technology, Gaithersburg, Maryland 20899-8541

**In this paper, we examine the regions of debonding between the fibers and the matrix surrounding fiber breaks formed during single fiber fragmentation tests. The fiber breaks are accompanied by areas of debonding between the matrix and the surface of the fiber. With increasing applied strain, the lengths of these debonded regions generally increase. At the end of the test, the matrix tensile strain adjacent to the debond regions is an order of magnitude higher than the applied strain (40% vs. 4%). Although the debond edges typically remain attached at the same locations on the fiber fragments, debond propagation along fiber fragments under increasing strain has been observed in some cases. The phenomenon is termed secondary debond growth, and two mechanisms that trigger secondary debond region growth have been proposed. As expected, tests with bare fibers and with fibers coated to alter interface adhesion indicate that the average size of debonded regions at the end of the test increases as the calculated interfacial shear strength decreases. However, a decrease in the “apparent” interfacial shear strength resulting from an increase in testing rate results in a decrease in the size of the average debond region. This result suggests an increase in the amount of energy stored in the matrix from the fiber fracture process. POLYM. COMPOS., 28:561–574, 2007. © 2007 Society of Plastics Engineers**

## INTRODUCTION

As previously noted [1], the single fiber fragmentation test (SFFT) procedure is the preferred micromechanics method for determining the interface stress transfer coefficient (I-STC) or interfacial shear strength (IFSS). In the SFFT, a dog bone is made with a high extension-to-failure resin and a single fiber embedded along the axis. The sample is pulled in tension by the application of sequential step-strains. When the matrix is strained, the stress is transmitted into the fiber through the fiber–matrix interface.

Since the fiber has a lower strain-to-failure than the resin, the fiber breaks—as the strain is increased—at the next inherent flaw that reaches its failure strength. When the embedded E-glass fiber fractures, a darkened region along the fiber–matrix interface accompanies the fiber fragmentation process. Depending on the strength and toughness of the fiber–matrix interface, the formation of matrix cracks perpendicular to the fiber axis may also accompany these darkened regions during fiber fracture. Examples of these features are shown in Fig. 1. These features have been observed previously by others for E-glass fiber SFFT specimens [2–6]. Although matrix crack formation is integrally associated with the fiber debonding process, we will focus, in this paper, only on the physics associated with fiber matrix debonding and defer discussion of matrix crack formation until a later manuscript.

Using a recently developed theory in optical physics that quantifies the transmission of light through an embedded fiber [7], detailed analyses of the fiber break regions, and research results from Galiotis and coworkers [8], these darkened regions with and without matrix crack formation will be reinterpreted in the discussion section as representing debonding at the fiber–matrix interface during the fiber fracture process. Fiber–matrix debonding is one of the internal material failure modes that precede macroscopic composite failure [9]. There is increasing evidence that composite failure may be rate dependent with the extent of this rate dependence being influenced by the characteristic viscoelastic behavior of the matrix in the fiber–matrix interface region. In the previous paper of this series [1], the fragment length distribution obtained from the SFFT of bare E-glass fibers (i.e., fibers not coated with any processing aids or silane coupling agents to promote adhesion) embedded in a DGEBA/*m*-PDA matrix was found to depend on the testing rate. Since the mean of the final fragment distribution is used to calculate an IFSS or I-STC, current models attribute such changes in the final fragment distribution to changes in the I-STC. It was also shown that the differentiation in fragment distributions with testing rate is evident at strain values much lower ( $\approx 2.5\%$ ) than the strain typically required to complete the test ( $\approx 4.2\%$ ). These results are consistent with the existence of stress concentrations at

Correspondence to: G.A. Holmes; e-mail: Gale.holmes@nist.gov  
Current address for R.C. Peterson is Corning, Inc., Manufacturing Technology and Engineering, Corning, New York 14831.  
DOI 10.1002/pc.20186  
Published online in Wiley InterScience (www.interscience.wiley.com).  
© 2007 Society of Plastics Engineers. \*This article is a US Government work and, as such, is in the public domain in the United States of America.

the end of broken fragments as described by Carrara and McGarry [10] and Jahankhani and Galiotis [11]. These stress concentrations can initiate failure of the fiber–matrix interface on the molecular level. This failure process can manifest itself in the following two ways: (a) additional complete debonding can occur at the initial fracture and debond site with increasing strain, and (b) a limited number of interface bonds can be broken in the intact fiber–matrix region adjacent to the initial fracture and debond site, without causing complete debonding. The second possibility can be viewed as a prelude to complete debonding. Therefore, prior to complete debonding the stress transfer efficiency of the intact fiber–matrix interface in the region adjacent to the fiber break can be reduced below its value prior to fracture. Both approaches have the net effect of increasing the average length of the fragments at saturation and reducing the derived I-STC.

In the previous paper [1], the final fragment distribution changed ( $325 \pm 79$  vs.  $379 \pm 91$ ) when the effective strain rate of the test was increased from  $2.5 \times 10^{-5} \text{ min}^{-1}$  to  $5.0 \times 10^{-5} \text{ min}^{-1}$ . Since the SFFT is performed by imposing sequential increments of strain, the effective strain rate is defined as the total strain at the end of the test divided by the total test time. Between the effective strain rates of  $5.0 \times 10^{-5} \text{ min}^{-1}$  and  $1.4 \times 10^{-4} \text{ min}^{-1}$ , changes in the fragment distributions were minimal. Similar tests have been performed by Netravali [12] on a variety of epoxy resin/graphite fiber systems. He found no correlation of the fragment distribution with testing rate. However, the slowest testing rate used by that author was  $7 \times 10^{-4} \text{ min}^{-1}$ . In contrast to the E-glass/epoxy resin results, fragment distributions for bare E-glass/polyisocyanurate SFFT specimens were found to be less sensitive to testing rate changes when tested over the same range of conditions used for the epoxy samples [1]. From these results it can be concluded that the factors that influence the rate dependence of the fiber–matrix interface strength are more complicated than the model envisioned from fundamental investigations relating the relaxation behavior of the matrix to strain. This is probably because the fiber–matrix interface has properties that differ from the bulk matrix. Since the interface is not formed until the composite is manufactured, it is not currently amenable to direct assessment. Hence, determination of the properties of the fiber–matrix interface and assessment of its deformation behavior have been the subjects of intense research. Investigations at NIST suggest that the rate dependence of the fiber–matrix interface is related to the existence of stress concentrations in the fiber–matrix interface region surrounding a fiber break, the strength of individual chemical bonds in the fiber–matrix interface region, and the rate that stress is relaxed in this region. Accordingly, increased viscoelastic relaxation of the matrix in the fiber–matrix interface region minimizes the magnitude of these stress concentrations. Decreasing the testing rate has the net effect of minimizing collateral damage to the intact fiber–matrix interface region adjacent to a fiber break and increasing the derived fiber–matrix interface strength.

In this paper, we continue our investigation of the failure processes associated with fiber breakage by investigating how debond region formation is influenced by strain rate and bonding strength. Conceptually, the size of the debond region formed during fiber fragmentation should vary inversely with the fiber–matrix interface strength. To verify this concept, the average size of the debond region generated from a strong interface (bare E-glass fibers) is compared to a weak interface (E-glass fibers coated with a silane coupling agent, *n*-octadecyl triethoxysilane, that bonds to the glass but not to the host matrix (i.e., non-bonding silane)). Since initial debond region formation is a fast fracture process, involving complete interface failure, the size of a debond region might not be test rate dependent.

## EXPERIMENTAL

### *Fiber and Mold Preparation*

To make single fiber fragmentation specimens, eight-cavity molds were prepared with RTV-664 from General Electric<sup>1</sup> following the procedure described by Drzal [13]. All molds were postcured at 150°C and rinsed with acetone prior to use. A 30 cm (12 inch) long tow of fibers was cut from a spool of E-glass (from Owens-Corning). The fibers were shown previously to be bare (i.e., no processing aids or sizings). The tow was washed with spectrophotometric grade acetone and vacuum dried at 100°C overnight and cooled. To alter the degree of bonding at the fiber–matrix interface, one tow of cleaned fibers was coated with the *n*-octadecyl triethoxysilane (NOTS) coupling agent prior to embedding. The coating procedure is described below. Single filaments of E-glass fiber were separated from the 30 cm tow, and care was taken to touch only the ends of the fiber. The central portion of the fiber was aligned down the central axis of each mold cavity with the aid of sprue slots. The fibers were temporarily fixed in place by pressing them onto double-stick tape. Small strips of double-stick tape were placed over each fiber end to hold them in place until permanently mounted by placing 5-min cure epoxy in the sprue slots.

### *Coating Procedure*

The acetone-cleaned fibers were either used as they were or suspended for 10 min in a graduated cylinder consisting of a solution with a mass fraction of 0.1% *n*-octadecyl triethoxysilane (NOTS) in 95% ethanol. The treated fibers were then removed from the silanol/ethanol solution and

---

<sup>1</sup>Certain commercial materials and equipment are identified in this paper to specify adequately the experimental procedure. In no case does such identification imply recommendation or endorsement by the National Institute of Standards and Technology, nor does it imply necessarily that the product is the best available for the purpose.

allowed to air-dry overnight. Subsequently, the treated fibers were placed in the molds as described above.

### Embedding Procedure

One hundred grams of diglycidyl ether of bisphenol-A (DGEBA, Epon 828 from Shell Chemical Co.) and 14.5 g of *meta*-phenylenediamine (*m*-PDA, Fluka Chemical Company) were weighed out in separate beakers. To lower the viscosity of the resin and melt the *m*-PDA crystals, both beakers were placed in a vacuum oven (Fisher Scientific Isotemp Vacuum Oven, model 281 A) set at 75°C. After the *m*-PDA crystals were completely melted, the silicone molds containing the fibers were placed into another oven (Blue M Stabiltherm, model OV-12A) that was preheated to 100°C. The preheated oven was turned off and the molds were heated for approximately 20 min. This last procedure dries the molds and minimizes the formation of air bubbles during the curing process.

At approximately 9 min before the preheated molds were removed from the oven, the *m*-PDA was poured into the DGEBA and thoroughly mixed. The mixture was placed into the vacuum oven and degassed for approximately 7 min. After removing the preheated molds from the oven, the mold cavities were filled with the DGEBA/*m*-PDA resin mixture using 10-cm<sup>3</sup> disposable syringes. The filled molds were then placed into a programmable oven (Blue M, General Signal, model MP-256-1, GOP). A cure cycle of 2 h at 75°C followed by 2 h at 125°C was used.

### Fragmentation Test

The fiber fragmentation tests were carried out on a small, hand-operated loading frame, similar to that described by Drzal [13], mounted on a Nikon Optiphot polarizing microscope. Before loading the specimen, the cross section dimensions of the gauge section were measured using a Mitutoyo electronic digital caliper. The standard uncertainty in these measurements is 0.005 μm. After mounting the specimen, the image was viewed using a CCD camera (Optronics LX-450 RGB Remote-Head microscope camera) and monitor (Sony, PVM-1344Q). Before the test, the fiber diameter was measured with an optical micrometer (VIA-100 from Boeckeler) attached to the video system. Nineteen measurements of the fiber diameter were taken along the fiber length. The standard uncertainty in these measurements is typically 0.3 μm. To measure debond locations or other points of interest in the sample, the sample was scanned by translating the loading frame under the microscope with a micrometer. The position of the load frame was monitored by a Linear Variable Differential Transducer (LVDT) (Trans-Tek, Inc. model 1002-0012). The LVDT position was digitized into the computer through an Analog-to-Digital board (Strawberry Tree, Inc.). The standard uncertainty in reproducibly relocating a point is 1.1 μm. Using propagation of error [14], the relative com-

bined standard uncertainty of the applied strains reported in Figs. 5–8 is 0.023%. The combined standard uncertainty of the debonds and fragment lengths given in Figs. 5–8 is 1.6 μm.

The specimens were tested by protocols designed to change the effective strain rate. In the fast and the slow test protocols the times between strain increments (dwell times) are 10 min and 1 h, respectively. For the intermediate (variable) test protocol, the initial dwell time is 10 min. After the first break the dwell time between subsequent strain increments increases because of the time required to measure all of the existing breaks. The load-time response of the matrix during these testing protocols has been given previously [1]. For these tests, nine bare E-glass fiber test specimens, denoted by Bare2\_x and Bare3\_x, and four specimens coated with NOTS, denoted NOTS\_dx, were used. The “Bare2” and “Bare3” labels refer to the second and third batches made of these specimens, respectively. The “NOTS\_d” nomenclature corresponds to the first batch of specimens made with this coupling agent. The “x” denotes the specimen number from a given batch. During the testing procedure, Bare2\_4 fractured before saturation was reached. A test was initiated on the Bare2\_8 specimen, but was halted prematurely. Since the Bare2\_8 specimen had been loaded to above 1.0% strain, it was not subjected to further testing.

In these experiments the debond regions were measured in the stressed and unstressed states. Since the matrix is viscoelastic, one cannot immediately return the specimen to the zero strain state to achieve zero stress in the matrix. Therefore, the specimen was unloaded to approximately zero stress and allowed to equilibrate for approximately 4–6 h. This process was repeated until no appreciable rise in the stress was observed during the 4–6 h period. A more detailed discussion of this phenomenon will be presented in a later manuscript.

## RESULTS AND DISCUSSIONS

### Debond Region Formation and Strain

During fragmentation experiments on bare E-glass/DGEBA/*m*-PDA SFFT specimens, darkened regions (between 15 μm and 30 μm long) form at the site of each fiber break (see Fig. 1). These regions have been observed by others [2–6], and also occur during the fragmentation of E-glass fibers in other matrices (e.g., polyisocyanurate and vinyl ester resins). To investigate debond region formation during fiber fracture an interpretation of the optical images that are represented in Fig. 1 is needed.

Prior to fiber fracture the transmission of light through the embedded fiber is governed by the following equation (see Ref. 15, Eq. 14):

$$T_s = 1 - \frac{2r_f}{w_s} Q_{ext}\{\rho\} = 1 - \frac{64\pi^2 r_f^3}{3w_s \lambda^2} |n^f - n^m|^2 \quad (1)$$

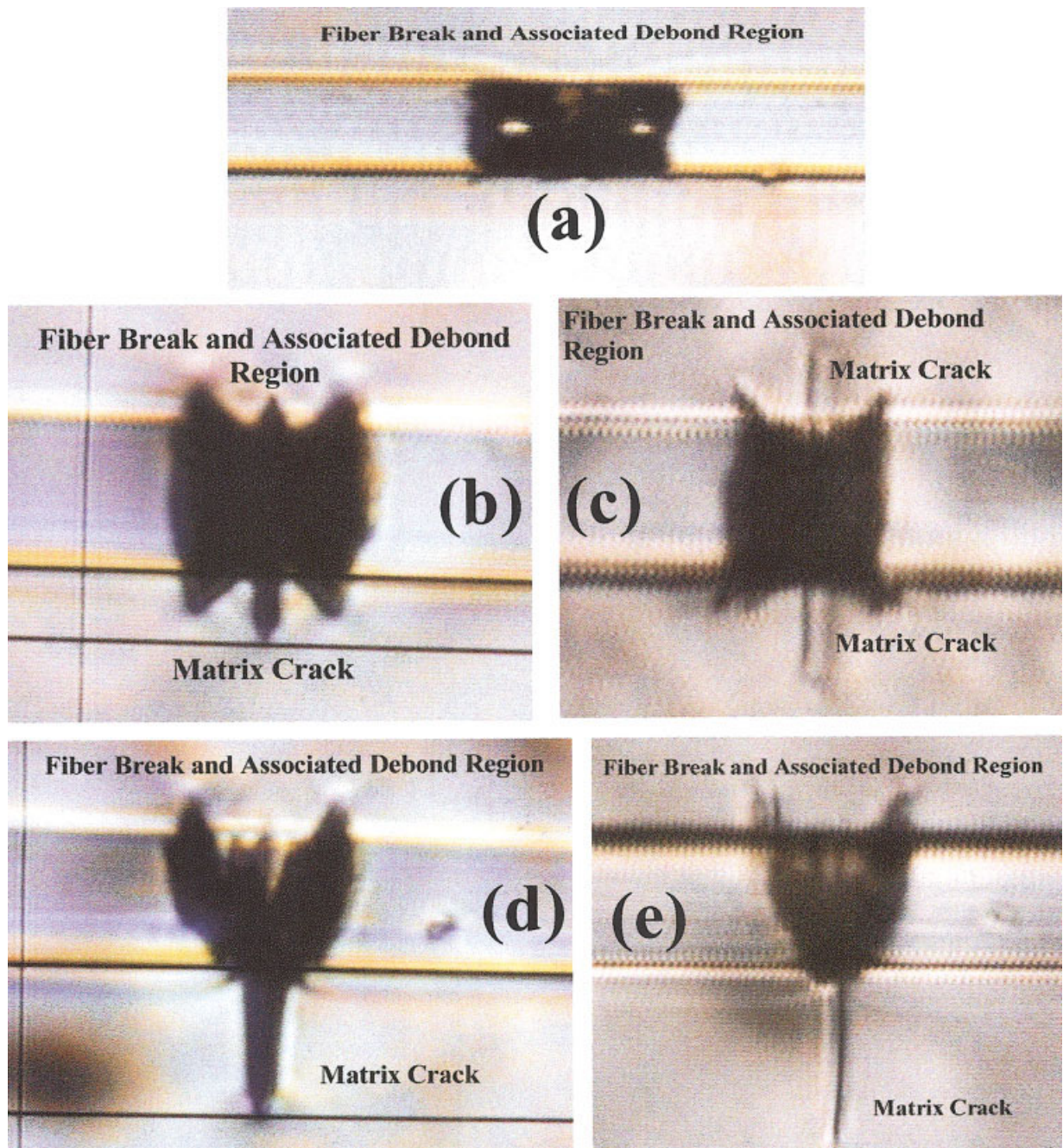


FIG. 1. Typical debond regions (a) debonding only, (b) debonding with disk shaped matrix crack (stressed), (c) debonding with disk shaped matrix crack (unstressed), (d) debonding with half-disk shaped matrix crack (stressed), and (e) debonding with half-disk shaped matrix crack (unstressed). [Color figure can be viewed in the online issue, which is available at [www.interscience.wiley.com](http://www.interscience.wiley.com)]

where

$T_S$  denotes the transmittance of a single-fiber composite,

$r_f$  denotes the radius of the embedded fiber,

$w_S$  denotes the width of the single-fiber composite,

$Q_{ext} \{ \rho \}$  denotes the efficiency factor for the transmission of light in a single-fiber composite and is a function of  $\rho$ ,

$\rho$  denotes the phase lag sustained by the central ray that passes through the fiber along a fiber diameter  $2r_f$  (see Fig. 2),

$\lambda$  denotes the wavelength of light, and

$n^f$  and  $n^m$  denote the index of refraction of the fiber and matrix, respectively.

The second form of the equation is obtained by assuming that  $Q_{ext} \{ \rho \}$  can be approximated by  $2\rho^2/3$  and substituting Eq. 12 in Ref. 15 for  $\rho$ . In Ref. 15, an explicit definition for the width of a single fiber composite,  $w_S$ , is not given. Hence it is not clear if  $w_S$  depends on the actual specimen thickness or on the intrinsic properties of the resin and the embedded fiber. Therefore, in Fig. 3, the transmittance of a single fiber com-

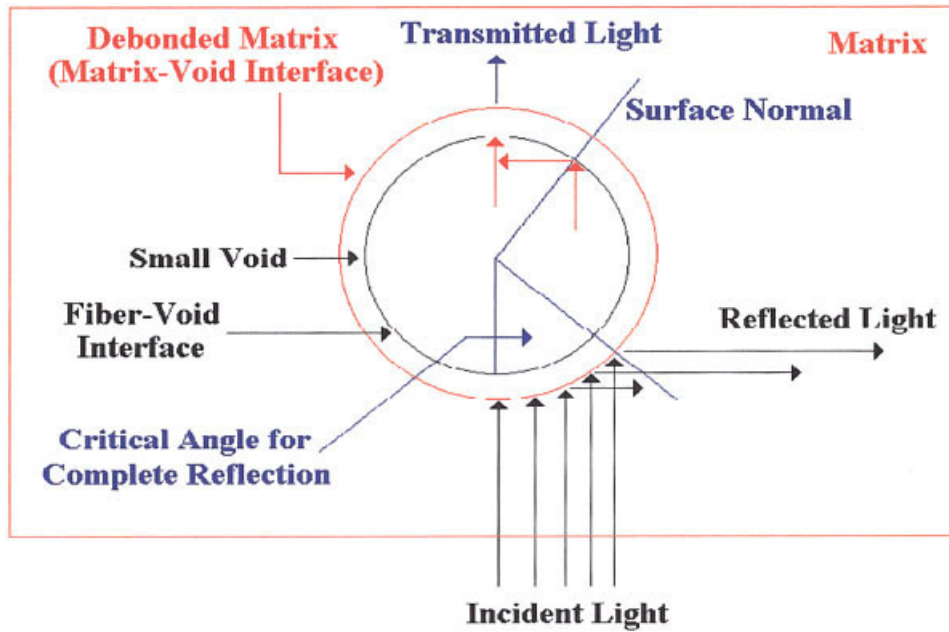


FIG. 2. Schematic of reflected light at debonded fiber–matrix interface. [Color figure can be viewed in the online issue, which is available at [www.interscience.wiley.com](http://www.interscience.wiley.com)]

posite, as predicted by the above equation, is given relative to the index of refraction difference between the matrix and the embedded fiber for single-fiber composite widths of 4 mm, 1 mm, and 0.1 mm. A fiber diameter of  $15\ \mu\text{m}$  and an incident wavelength of light of 589 nm are assumed. As  $w_s$  decreases, the maximum difference in index of refraction required to achieve zero transmittance also decreases. Hence, this equation

holds for the cases where  $r_f \gg \lambda$  and the refractive index of the fiber is very close to the refractive index of the matrix ( $n^f \cong n^m$ ). For the latter condition, the reflection and refraction of the light rays at the interface between the fiber and the matrix and the condition of polarization can be neglected. Therefore, the reduction of transmitted light at the fracture site involves physics that violates the conditions of the above equation.

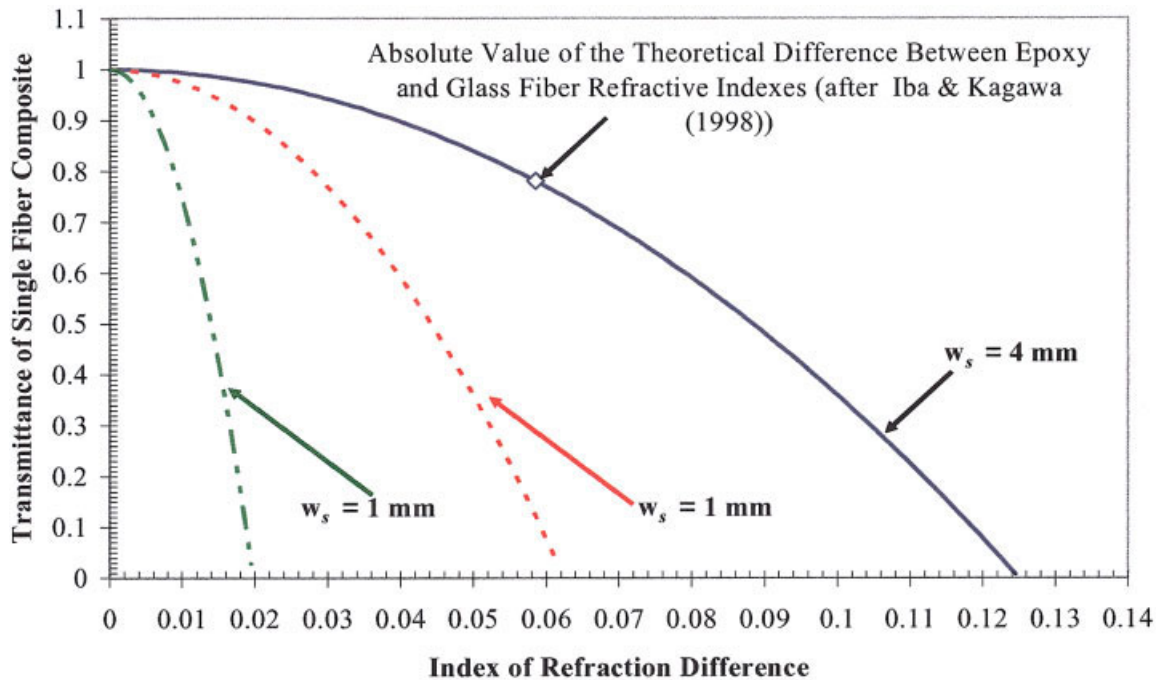


FIG. 3. Effect of specimen width on light transmission through a single fiber composite. [Color figure can be viewed in the online issue, which is available at [www.interscience.wiley.com](http://www.interscience.wiley.com)]

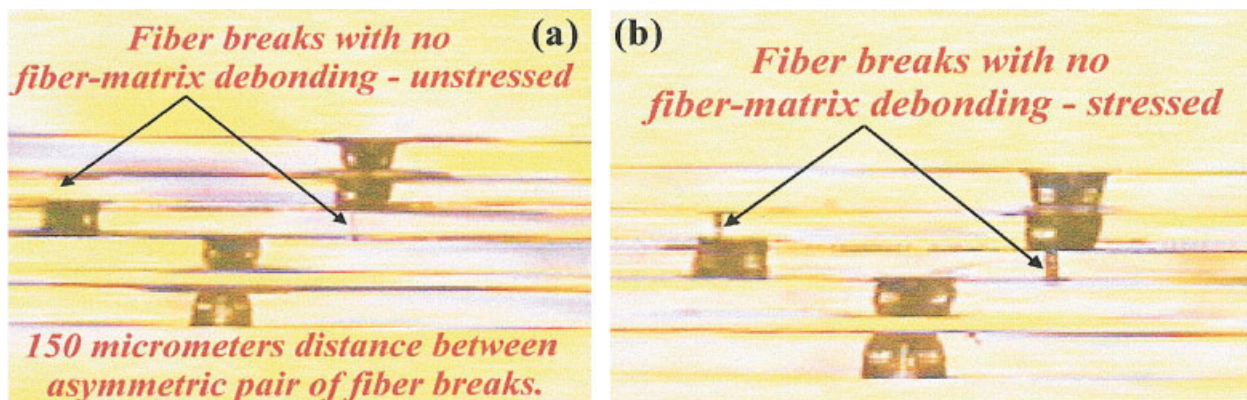


FIG. 4. Fiber breaks with no fiber–matrix debonding (a) unstressed; (b) stressed. [Color figure can be viewed in the online issue, which is available at [www.interscience.wiley.com](http://www.interscience.wiley.com)]

The reduction in transmitted light through the darkened region surrounding the fiber break may be explained by the existence of a small gap caused by the complete debonding of the matrix from the fiber. Since the break around the fiber will be circular, conditions for total internal reflectance will be realized at the matrix–gap interface and at the fiber–gap interface (see Fig. 2) at angles greater than  $40^\circ$  to the impinging surface. Because the transmitted light gradually decreases up to the  $40^\circ$  critical angle for total internal reflection [15], the maximum transmitted light should be from the light rays that impinge perpendicular to the surface. In Fig. 1a, the two eyelets reflect this condition. The sharp transition from light-to-dark along the fiber in the fiber break region is therefore taken by the authors to consist of areas of bonding and complete debonding, respectively, at the fiber–matrix interface or interphase. Based on the above observations and assumptions, the bonding–debonding transition delineated by the sharp change from light-to-dark is fixed at a specific location on the fiber surface.

The most convincing evidence for this interpretation can be found in Fig. 4. In Fig. 4a, multiple unstressed fractured fibers with debonding are shown. Also delineated in this figure are two fibers that exhibit multiple fractures along their lengths. These fiber fracture sites are readily visible when stressed (see Fig. 4b), with a dark gap occurring between the fractured ends of each fiber. Therefore, the second fractures that are only visible under stress occurred without debonding. The occurrence of these fracture sites suggests that the strain is high and stress state complex in the matrix surrounding these breaks, since a simple strain analysis would suggest that the strain and stress states in these regions are infinite. Noting that when the fibers are unstressed the fracture ends touch and are barely visible, one can readily infer that the remaining darkened regions in the unstressed state are due to fiber–matrix debonding.

Additional support for this interpretation is found in Fig. 5. In this figure, the evolution of a debond region's length

(debond region #39 from specimen Bare2\_1) during the fragmentation process is shown versus increasing strain. For comparison, the average lengths of all the debond regions are also shown versus increasing strain (solid line). These data were extracted from the fragmentation map generated in Ref. 1. Of particular interest in Fig. 5 is the size of a debond region at the end of the fragmentation test in the stressed and unstressed states. On average, the debond length is approximately  $24\ \mu\text{m}$  in the stressed state ( $26.2\ \mu\text{m}$  for debond region #39), while the average debond length is approximately  $17\ \mu\text{m}$  ( $17.9\ \mu\text{m}$  for debond region #39) in the unstressed state. From the experimental section, the standard uncertainty in the above debond lengths is  $1.6\ \mu\text{m}$ . Hence, the changes in debond lengths upon release of the stress after saturation is significant ( $p\text{-value} < 0.001$ ). For these SFFT specimens, the increase in length of a debond region with increasing applied strain implies that there is a large, localized matrix strain.

As previously stated, the residual strain in an E-glass/DGEBA/*m*-PDA epoxy resin specimen is approximately 0.2%. If the residual strain is assumed to reside completely in the debond regions between the fiber breaks, a global residual strain of 0.21% in the Bare2\_1 specimen reflects an average residual strain in the debond regions of 5%. This calculation implies that the high strains in the debond regions at the end of the test in this E-glass/DGEBA/*m*-PDA specimen are achieved with minimal permanent damage to the network structure. Making the assumption that the bond–debond interface is fixed at a specific location on the fiber (i.e., no optical effects occur that will cause the debond region to shrink), then the average matrix tensile strain in the debond regions is approximately 41%, while the global strain in the matrix is only 4.2%. Although this high average strain is approximately six times the failure strain of the bulk matrix under uniform tensile loading, localized strains in epoxy resins as high as 50% have been reported [16]. The 41% strain translates into an average gap at saturation of  $7\ \mu\text{m}$  between the ends of the fiber fragments ( $8.3\ \mu\text{m}$  for debond region #39 in Fig. 5).

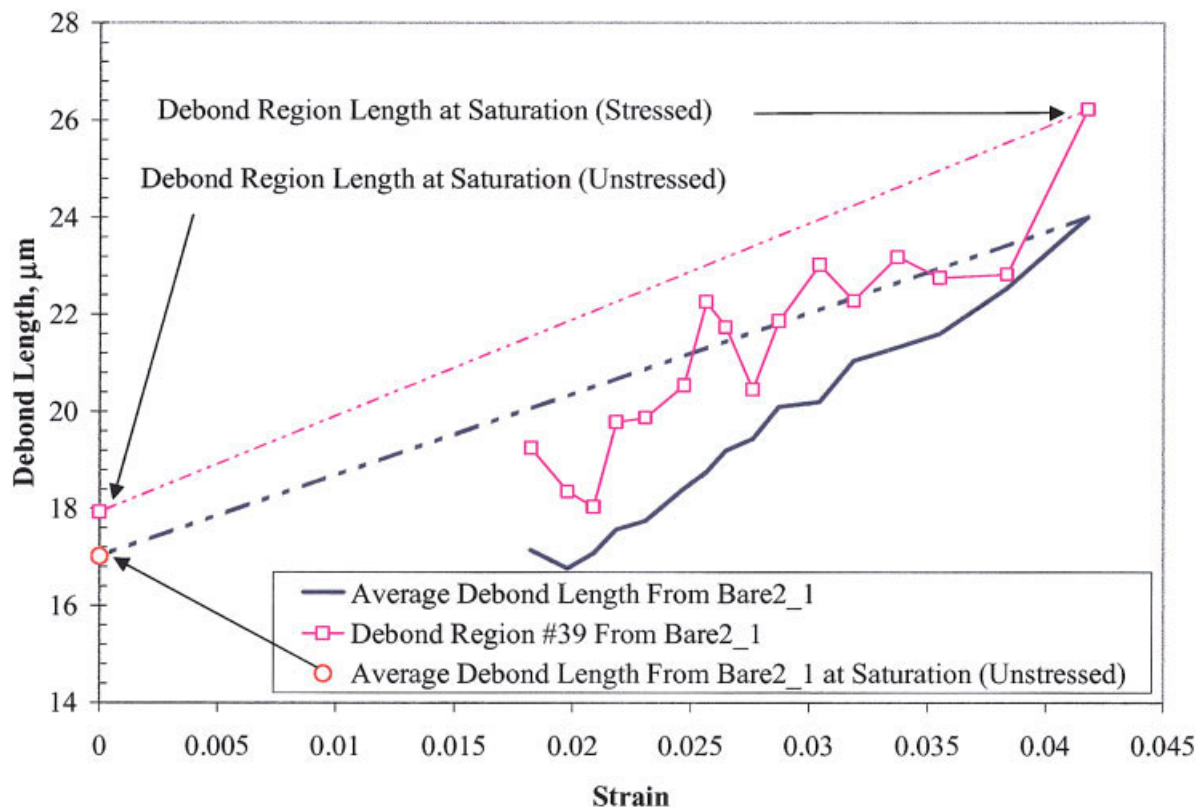


FIG. 5. Evolution of debond region #39 and average debond length with strain for fragmentation data from Bare2\_1. [Color figure can be viewed in the online issue, which is available at [www.interscience.wiley.com](http://www.interscience.wiley.com)]

### Secondary Debonding After Initial Debond Region Formation

Research by Galiotis and coworkers [8] on a carbon fiber/epoxy resin system has shown that additional debonding at the fiber–matrix interface occurs with increasing strain (secondary debond growth) after the initial fiber break. For debond regions associated with early fiber breaks their data indicates that secondary debond region growth can be as much as 100  $\mu\text{m}$  at saturation ( $\approx 5.0\%$  strain). Similar behavior has been observed at the NIST laboratory

on carbon fibers embedded in DGEBA/*m*-PDA epoxy resin systems. For the E-glass/DGEBA/*m*-PDA epoxy resin systems being investigated here, the average debond region length at saturation ( $\approx 4.2\%$  strain) is typically less than 35  $\mu\text{m}$  (see Table 1). Since the unstressed length of a newly formed debond region is about 17  $\mu\text{m}$ , evidence of secondary debonding after initial fiber fracture in the E-glass/DGEBA/*m*-PDA epoxy resin systems can only be detected by comparing the final unstressed debond length with the stressed length of the debond region when initially formed.

TABLE 1. Average debond region statistics at saturation.

Test specimen and test condition	Average debond lengths ( $\mu\text{m}$ )		Global strain at saturation (%)	Average debond strain at saturation (%)	Debanded fiber (%)
	Unstressed	Stressed			
Bare2_1 intermediate	17.01 $\pm$ 2.20	24.01 $\pm$ 2.85	3.98	41	4.3
Bare2_2 intermediate	16.29 $\pm$ 1.84	23.33 $\pm$ 2.41	4.04	43	4.3
Bare2_3 intermediate	15.34 $\pm$ 1.73	20.85 $\pm$ 2.27	3.56	35	3.9
Bare2_5 intermediate	15.16 $\pm$ 1.65	21.39 $\pm$ 2.19	3.53	41	3.6
Bare2_6 slow	15.47 $\pm$ 1.65	22.70 $\pm$ 2.43	4.27	46	4.6
Bare2_7 slow	17.70 $\pm$ 1.50	23.39 $\pm$ 1.76	4.01	32	5.2
Bare2_9 slow	18.83 $\pm$ 2.16	26.11 $\pm$ 2.44	4.20	39	5.2
Bare2_10 slow	17.16 $\pm$ 1.61	21.78 $\pm$ 2.56	4.08	27	5.1
Bare3_1 fast	18.06 $\pm$ 2.99	26.11 $\pm$ 4.10	4.50	45	4.7
NOTS_d1 intermediate	24.56 $\pm$ 3.35	32.60 $\pm$ 4.29	3.36	33	3.5
NOTS_d2 intermediate	25.02 $\pm$ 3.95	33.81 $\pm$ 4.54	3.78	35	4.0
NOTS_d3 intermediate	27.19 $\pm$ 6.08	36.37 $\pm$ 6.52	3.46	34	3.5

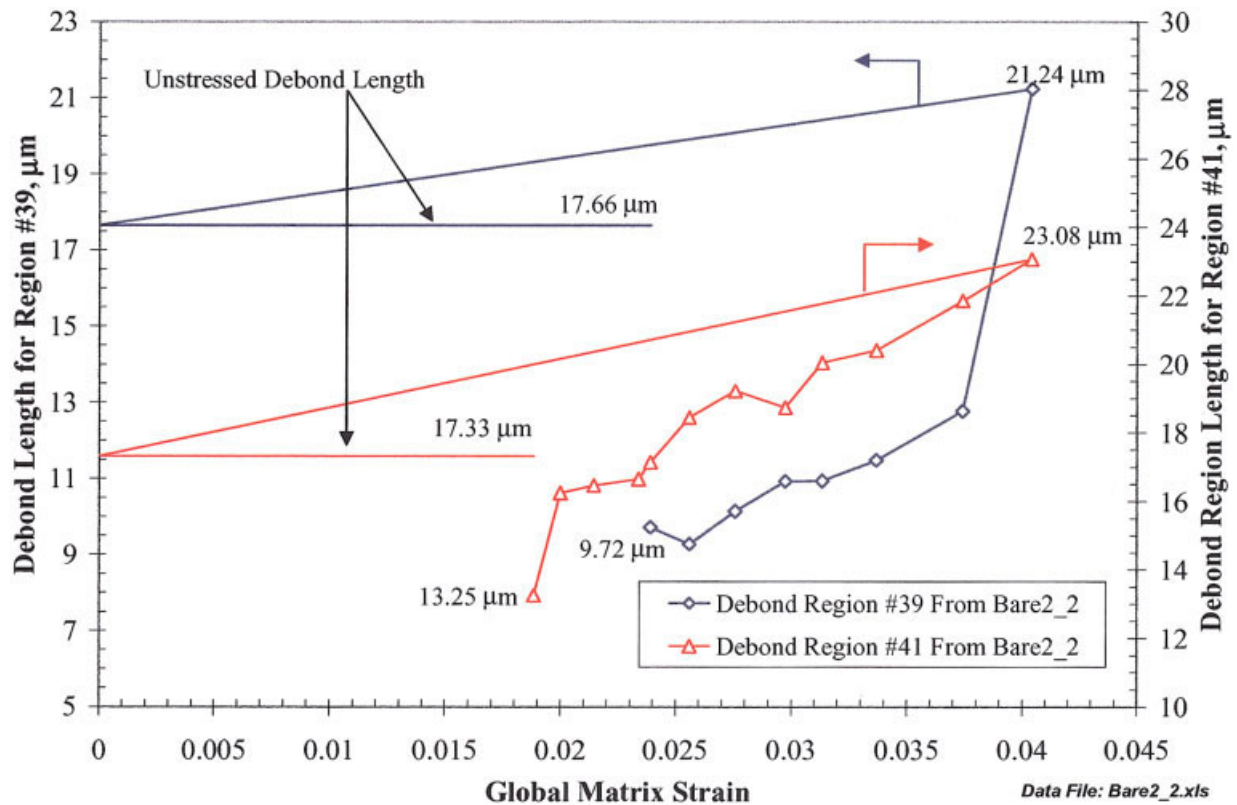


FIG. 6. Evolution of two debond regions from Bare2\_2. [Color figure can be viewed in the online issue, which is available at [www.interscience.wiley.com](http://www.interscience.wiley.com)]

When the unstressed length of a debond region at saturation is greater than the stressed length at formation, additional growth of the debond region after its initial formation is indicated (i.e., secondary debond region growth). Two examples of secondary debond region growth after initial formations are shown in Fig. 6. In this figure, debond regions 39 and 41 from specimen Bare2\_2 are shown to increase at least 7.9  $\mu\text{m}$  and 4.1  $\mu\text{m}$ , respectively, after formation. Since the maximum standard uncertainty in each debond length is 1.6  $\mu\text{m}$ , these increases are significant.

For debond region 41 most of the secondary growth (3  $\mu\text{m}$ ) seems to occur during the first strain increment (strain = 0.0200) after formation. At this strain increment, debond region 41 is surrounded by fiber fragments of 6964  $\mu\text{m}$  and 9200  $\mu\text{m}$  in length. On the next strain increment the 6964  $\mu\text{m}$  fragment fractures into four fragments of 4188  $\mu\text{m}$ , 1906  $\mu\text{m}$ , 351  $\mu\text{m}$ , and 470  $\mu\text{m}$ . Since all of these fragments occurred during the same strain increment, in only one case can it be assumed for certain that debond region 41 is adjacent to the parent fragment. Even with this uncertainty, it is reasonable to assume that additional debond region growth occurs at the 0.0200 strain when the 6964  $\mu\text{m}$  parent fragment fractures. During the course of the experiment, at least five additional fracture events are known to occur where debond region 41 is adjacent to the parent fragment. These additional fracture events may give rise to the additional debond region growth ( $\approx 1.0 \mu\text{m}$ ) detected at this debond site.

In contrast, six strain increments are required for debond region 39 to exhibit an apparent increase in length of 3.5  $\mu\text{m}$ . During these strain increments only one fracture event occurs where debond region 39 is adjacent to the parent fragment. In this fracture event debond region 38 is formed (strain = 0.0297). Debond region 38 measured 20.97  $\mu\text{m}$  in length at formation and at least 22% of that length is due to matrix strain since the unstressed length of this debond region at saturation is 17.15  $\mu\text{m}$ . Debond regions 39 and 37 (which are adjacent to the parent fragment that fractured to generate debond region 38) exhibited only modest increases in size ( $< 1 \mu\text{m}$ ) during the fracture event to generate debond region 38. Since the standard uncertainty in a debond length measurement is 1.6  $\mu\text{m}$ , this change is within experimental uncertainty. The lack of evidence supporting secondary debond growth at debond regions 39 and 37 during the fracture event that generated debond region 38 may be related to the size of the parent fragment and the amount of excess strain energy in the fragment before fracture. The size of the parent fragment that generated debond region 38 was only about 756  $\mu\text{m}$ .

Using 9.28  $\mu\text{m}$  (debond region size at strain = 0.0256) as the reference length for debond region 39, the strain at the next to the final strain increment is approximately 38%; however, without assuming additional debond region growth the strain at the final strain increment would be 129%. The unstressed length of debond region 39 after the final strain increment indicates that the debond strain is only

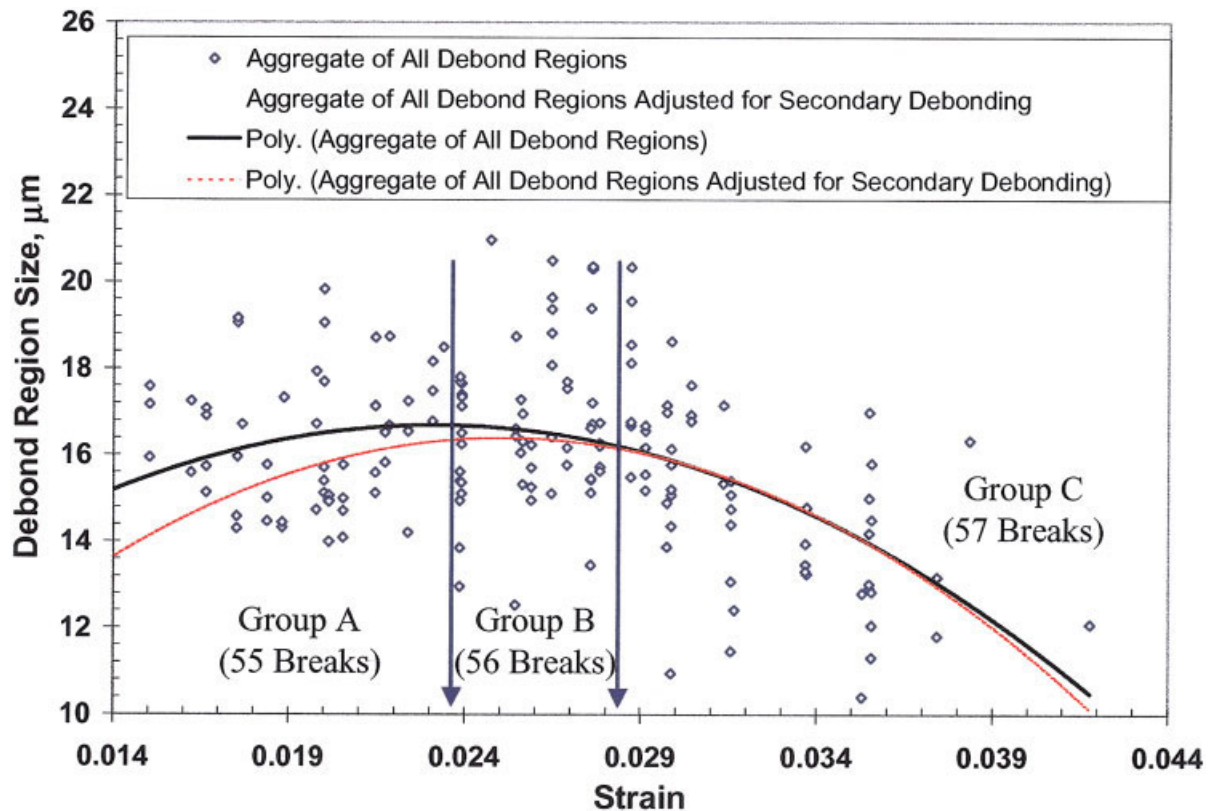


FIG. 7. Aggregate of unstressed debond regions from intermediate test protocol specimens. [Color figure can be viewed in the online issue, which is available at [www.interscience.wiley.com](http://www.interscience.wiley.com)]

20%. Since the stressed length of debond region 39 before the last strain increment is  $12.8 \mu\text{m}$  and the unstressed length after the last strain increment is  $17.7 \mu\text{m}$ , it is plausible that most of the debond region growth in debond 39 occurs on the last strain increment.

Therefore, at least two triggering mechanisms appear to be active in generating secondary debond region growth at existing debond region sites. In larger fragments, there appears to be enough excess strain energy to generate a debond region at the fracture site and promote secondary debond growth at the two preexisting debond sites that are adjacent to the parent fragment. For smaller fragments secondary debond growth may occur when the matrix material in the debond region has the potential of reaching very high strains. The controlling factors in both mechanisms may be the degree of initial damage sustained by the intact interface region adjacent to the initial fracture and debond site and the existence of higher shear stresses in this region caused by stress concentrations.

#### *Correlating Debond Region Size With Strain at Formation*

Since matrix strain contributes a significant amount to the apparent growth of a debond region with increasing applied strain, the unstressed lengths of the debond regions at their respective formation strains are plotted in Figs. 7

and 8. Unlike the average unstressed fragment lengths which show a clear delineation in size with testing protocol [1], the variation of the unstressed debond lengths within a testing protocol exhibits considerable variability. However, with and without adjustments made for secondary debonding the unstressed debond averages from three of the intermediate test protocol specimens (Bare2\_2, 3, and 5) are distinctly different from three of the four debond averages obtained from the slow test protocol specimens (Bare2\_7, 9, and 10) (see Table 1). Therefore, analysis of the data in this section focuses on the aggregate data from each test protocol to discern general trends that may exist.

Therefore, each plot in Figs. 7 and 8 is an aggregate of the data points from the respective intermediate and slow test protocol specimens. Because of the finite size of each step-strain, multiple fracture events are often recorded at the same applied strain. To aid the eye in discerning possible trends that exist in the data two second-order polynomial trendlines are plotted on each figure. Since the model developed by Nairn and Liu [17] predicts a maximum in the size of the debond regions prior to the saturation strain, a second-order polynomial trendline was chosen to capture this effect if present. The solid trendline corresponds to the measured unstressed debond lengths obtained at the end of each test. The corresponding data points for these measured lengths are plotted. The average-unstressed debond value for each test specimen is recorded in Table 1.

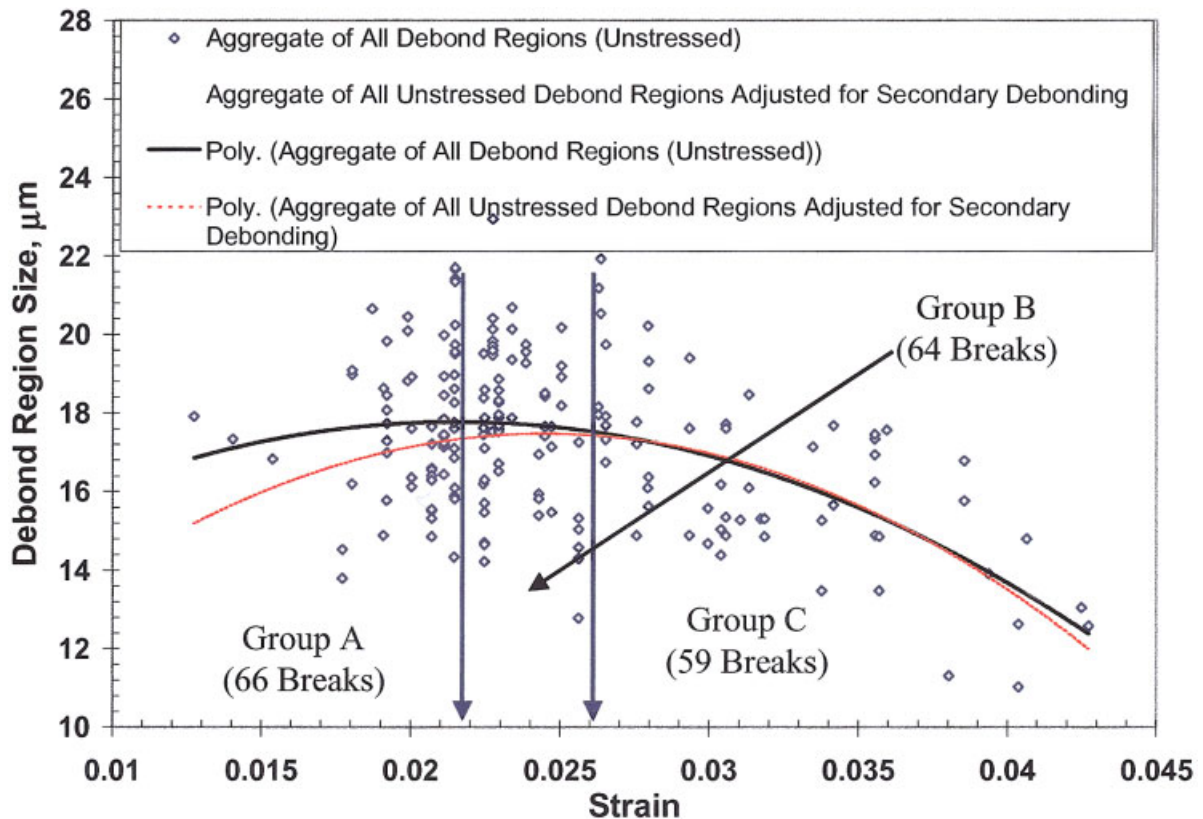


FIG. 8. Aggregate of unstressed debond regions from slow test protocol specimens. [Color figure can be viewed in the online issue, which is available at [www.interscience.wiley.com](http://www.interscience.wiley.com)]

Since secondary debonding has been shown to occur after formation of the initial debond regions during fiber fragmentation, the thin dashed trendline was obtained by substituting for those points that indicated secondary debonding the value of the stressed debond length at the time of fracture. For example, the solid trendline in Fig. 7 would include the unstressed measured lengths of  $17.66 \mu\text{m}$  and  $17.33 \mu\text{m}$ , respectively for debond regions #39 and #41 shown in Fig. 6 from the Bare2\_2 datafile. In the dashed trendline these data points would be replaced with the length of the debond regions at formation (i.e.,  $9.72 \mu\text{m}$  and  $13.25 \mu\text{m}$ , respectively; see Fig. 6). To maintain clarity in the figures (i.e., Figs. 7 and 8), the modified data points are not shown in each figure.

To support the use of the second order polynomial trendlines, the data points in each figure were subdivided into three approximately even groups in terms of the number of debond regions, with the restraint that the multiple debonds that occurred in a given strain were never divided between two regions. For the specimens tested by the intermediate test protocol, this resulted in the 168 data points in the aggregate set being divided into three groups of 55, 56, and 57 data points. The aggregate and individual groups were tested first for normality using the skewness and kurtosis ratios and then for homogeneity of variances by the Levene's test at a 10% significance level. All groups, except for Group B when adjusted for secondary debonding, con-

formed to the normality and homogeneity of variances conditions. Group B when adjusted for secondary debonding was found to be non-normal in the kurtosis ratio (k.r. = 3.20: normality values for this and the skewness ratio occur between  $-2.00$  to  $2.00$ ). Exclusion of the  $9.72 \mu\text{m}$  value for debond region #39 (see Fig. 6) resulted in a normal kurtosis ratio of 0.60.

However, it should be noted that the inclusion or exclusion of the  $9.72 \mu\text{m}$  data point, with the exception of slightly changing the  $p$ -value, had no affect on the conclusions obtained from the analysis of variance analysis (ANOVA) of this data. The debond lengths in Group C when compared to Groups A and B, were found to be statistically smaller ( $p$ -values  $< 0.0007$ ), except when Group C and Group A were adjusted for secondary debonding. In this case, ANOVA comparing Groups C and A yielded a  $p$ -value of 0.068, while the ANOVA between Groups C and B indicated that these two groups were still statistically different with a  $p$ -value of 0.0002. The shift in significance between Groups C and A when secondary debonding is accounted for arises from the fact that 49% of the 55 data points in Group A were adjusted to smaller values, while only 7% were adjusted in Group C. Based on the above analysis, the use of second order polynomial trendlines for the intermediate test protocol specimens is consistent. For completeness only 21% of the debond region values were adjusted in Group B.

ANOVA of the 189 debond regions for the slow test protocol specimens, where they were divided into groups of 66, 64, and 59, yielded similar conclusions (see Fig. 8). In Groups A, B, and C, 47%, 28%, and 8%, respectively, of the debond values were adjusted when secondary debonding was considered. While the extent of secondary debond region growth seems to decrease from Group A to C in the slow test protocol specimens (averages 1.3, 1.1, 0.5, respectively), constant values were observed in the intermediate test protocol specimens (i.e., average equals 1.4, 1.2, and 1.5, respectively).

The adjusted trendlines in Figs. 7 and 8 indicate that the average length of a debond region increases with increasing strain up to approximately 2.7% strain and then trends downward. The upward trend in the initial size of a debond region with increasing strain is consistent with Galiotis' experimental results [8] on carbon/epoxy model composites which showed that the initial length of a debond region is related to the strain energy of the fractured fragments; that is, the initial length of a debond region formed during fiber fracture at low strains is smaller than the initial length of a debond region formed during fiber fracture at higher strains. As mentioned in the previous section, the lengths of the debond regions formed at small strains were found by Galiotis to be comparable at saturation with debond regions formed at higher strains. Therefore, Galiotis' data indicates that secondary debonding can occur at an existing debond site as the strain is increased. For a debond region formed at a low strain, Galiotis data indicates that secondary debond region growth is appreciable only above a critical strain value. For the carbon/epoxy model composite investigated by Galiotis the critical strain value was approximately 1.6% (see Fig. 16a in Ref. 8).

Theoretical calculations by Nairn and Liu [17], also using carbon/epoxy data, indicate that the initial debond length associated with a newly formed fiber break does increase initially with increasing strain during fragmentation. However, their theoretical calculations indicate that a maximum is reached before saturation. Hence, the initial size of the debond regions associated with fiber breaks near saturation decreases with increasing strain. Although the predictions of the Nairn–Liu model are consistent with the experimental results presented here for a glass/epoxy model composite, the model developed by Nairn and Liu equates the total energy released by fiber fracture and debonding to the total energy required to create the new fiber fracture and debond fracture surfaces. These authors acknowledge that other energy dissipation mechanisms are possibly active during fiber fragmentation. As was shown in the previous section, the strain energy in the debond regions increases as the matrix strain is increased. This dissipation mechanism may need to be accounted for before an accurate measure of the debond toughness is obtained.

Support for this assertion can be found in the comparative plot of the trendlines of the debond region data from the intermediate and slow test protocol test specimens (see Fig. 9). This plot indicates that on average the debond lengths

from the slow test protocol specimens are larger than the debond lengths from the intermediate test protocol specimens by a constant difference of approximately 1  $\mu\text{m}$ . Consistent with Fig. 9, ANOVA of the aggregate data sets for the unadjusted and adjusted debond lengths indicate a statistically significant difference ( $p$ -value  $< 9.0\text{E}-9$ ) of approximately 1.3  $\mu\text{m}$  between the intermediate and slow test protocol specimens. Since the strains at saturation were comparable between the two testing protocols and the amount of energy dissipated by debonding is reflected in the average size of the debond regions, this statistical difference suggests that more energy went into fiber–matrix debonding in specimens tested by the slow test protocol than specimens tested by the intermediate test protocol.

All things being equal these data further indicate that more of the strain energy released during fiber fracture is stored in the matrix of the intermediate test protocol specimens. Using an approach suggested by a reviewer, a crude estimate of the energy dissipated in the matrix during fiber fracture can be obtained using the Kelly–Tyson model [18]. In Fig. 10, the fiber before and after fragmentation is shown with the stress build-up near the break in the fiber fragments approximated by the Kelly–Tyson model. In this figure the following symbols are used:

$2l$  denotes the fragment length affected by the fiber break,

$l_T$  denotes the stress transfer length,

$l_u$  denotes the unbonded, stress free length of fiber fragment in the break region,

$2g$  denotes the total gap between fiber ends,

$2d$  denotes the total dark region, and

$\epsilon_g$  denotes the global strain at the time of fiber fracture.

From arguments in the previous section we can assume that the matrix remains connected to the fiber at the debond region boundary. In addition, the debonded region after fiber fracture is assumed to consist of fiber debonded from the resin and a gap between the two fiber fragment ends. This assumption is supported by Figs. 4 and 5, where the decrease in the size of the debond region after the applied strain is removed is shown. As an example, the size of debond region 38, discussed above, at formation was 20.97  $\mu\text{m}$  and 17.15  $\mu\text{m}$  after removing the applied strain.

From Fig. 10 and the above assumptions, it can be shown that  $l$ ,  $l_T$ , and  $d$  have the following forms:

$$l = l_o(1 + \epsilon_g) = l_T + d \quad (2)$$

$$l_T = (l_o - l_u) \left( 1 + \frac{\epsilon_g}{2} \right) = \frac{\epsilon_g l_c}{\epsilon_s 2} = \frac{2\epsilon_g}{3\epsilon_s} (l_s) \quad (3)$$

$$d = l_u(1 + \epsilon_{mb}) \quad (4)$$

where

$2l_o$  denotes the unstrained length of the fiber segment affected by the fiber break,

$l_c$  denotes the critical transfer length at saturation,

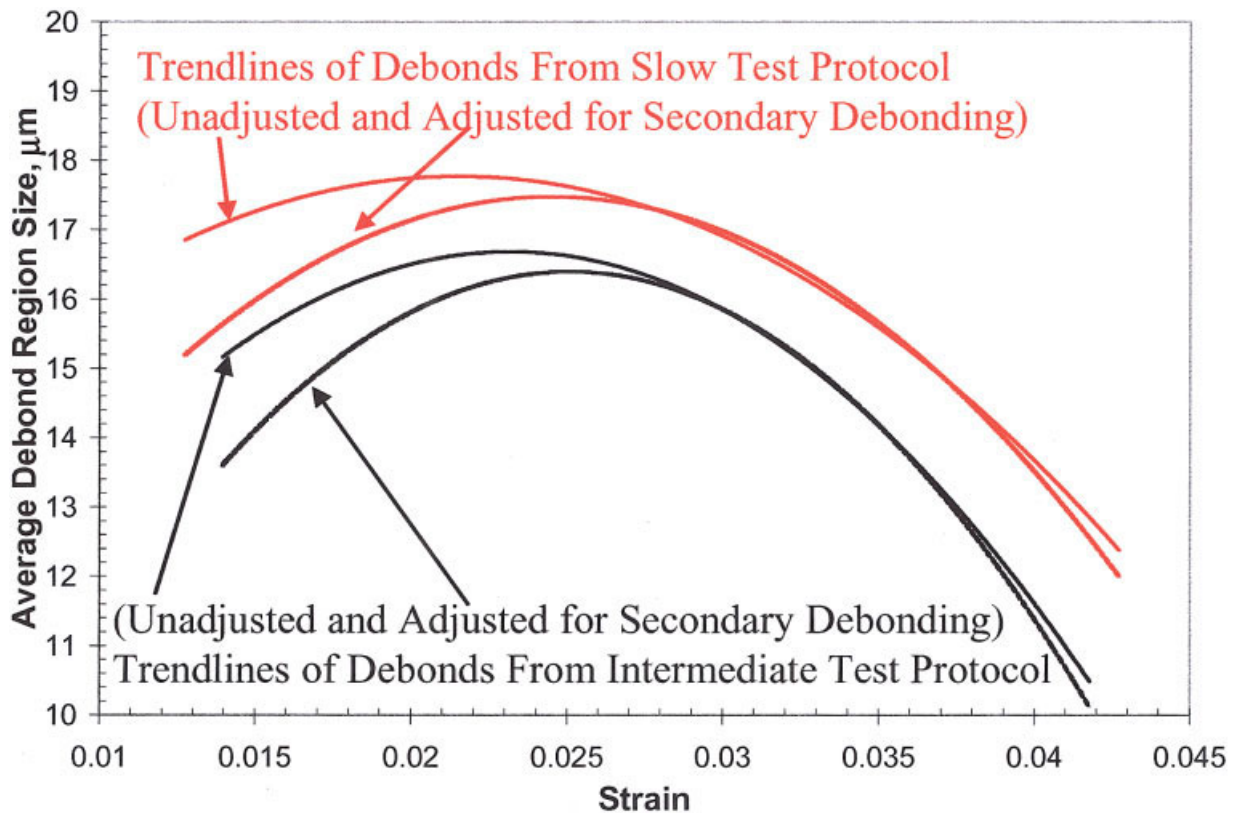


FIG. 9. Comparative plot of trendlines from intermediate and slow test protocol specimens. [Color figure can be viewed in the online issue, which is available at [www.interscience.wiley.com](http://www.interscience.wiley.com)]

$\langle l_s \rangle$  denotes the average fragment length at saturation,  $\epsilon_s$  denotes the global strain at saturation, and  $\epsilon_{mb}$  denotes the matrix strain in the fiber break region.

The expression for  $l_T$  is a direct result of the Kelly–Tyson constant shear stress approximation, the assumption that the strain build-up in the stress transfer region during the test is the same as the strain build-up at saturation, and the use of  $l_c = (4/3)\langle l_s \rangle$ .

Solving for  $l_u$  using the first variant of Eq. 3, the following equation can be obtained by substituting the two variants of Eq. 2 for  $l_0$  and  $l$  and then substituting the third variant of Eq. 3 for  $l_T$ :

$$l_u = \frac{1}{(1 + \epsilon_g)} \left[ d + \left( \frac{2\epsilon_g}{3\epsilon_s} \langle l_s \rangle \right) \left( 1 - \frac{1 + \epsilon_g}{1 + \frac{\epsilon_g}{2}} \right) \right]. \quad (5)$$

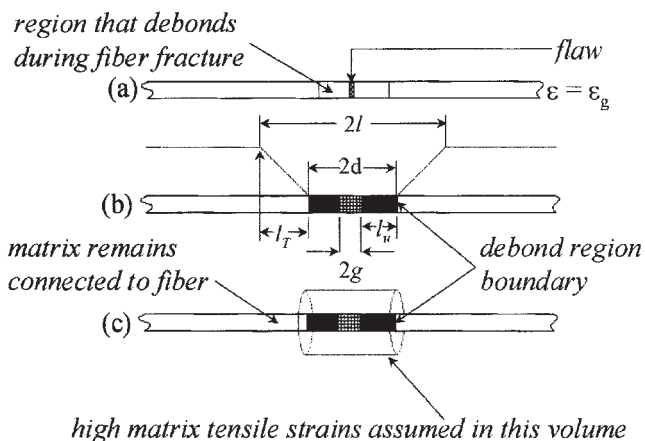


FIG. 10. Schematic of fiber fracture and matrix debonding: (a) before fracture, (b) after fracture, (c) model used to calculate energy absorbed by matrix.

Therefore,  $l_u$ —the unbonded stress free length of fiber fragment in the fiber break region—can be expressed approximately in terms of measurable parameters. As an example, if  $\langle l_s \rangle = 325 \mu\text{m}$ ,  $2d = 20 \mu\text{m}$ ,  $\epsilon_g = 0.02$ , and  $\epsilon_s = 0.04$ , then  $l_u = 8.75 \mu\text{m}$ . This calculated size of  $l_u$  agrees well with the unstressed measures of the total debond lengths found in the bare E-glass fiber specimens (see Table 1). Using Eq. 4, the matrix strain in the fiber break region,  $\epsilon_{mb}$ , is estimated to be 14%. It follows that the gap between the fiber ends,  $2g$ , at the 2% failure strain is estimated to be  $5.0 \mu\text{m}$ . Previously, the average debond strain in region #38, discussed above, was estimated to be 22% with a  $2g$  value of  $3.8 \mu\text{m}$ . Hence, this crude approximation appears to generate consistent estimates for the debonding caused by fiber fracture and the average distance between the fiber ends.

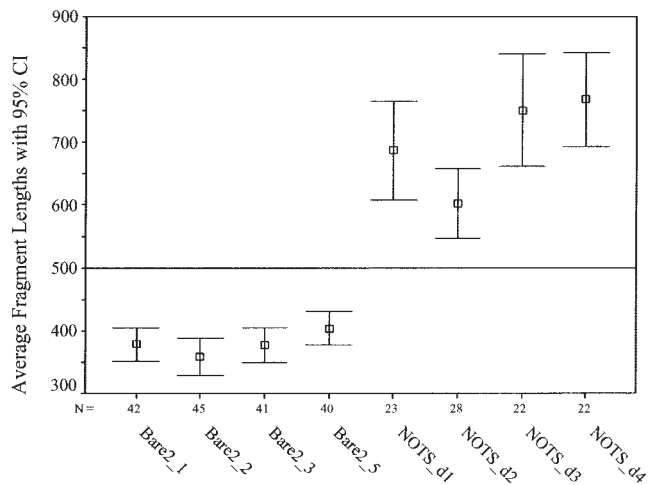


FIG. 11. Mean plot of unstressed fragment lengths with 95% confidence intervals. All specimens were tested using the intermediate test protocol. The NOTS specimens are E-glass fibers coated with *n*-octadecyl triethoxysilane coupling agent.

Furthermore, if the high strains in the debond region are assumed to be encased in a cylindrical volume of resin that is 20  $\mu\text{m}$  long and radiates 10  $\mu\text{m}$  out from the fiber (see Fig. 10c), the strain energy in the matrix is  $2.6 \times 10^{-7}$  J. For this calculation, the matrix yield stress can be taken to be 100 MPa. From Nairn's research, the fracture energy generated for a 10  $\mu\text{m}$  carbon fiber is  $(1.4 \text{ to } 3.1) \times 10^{-6}$  J, with the lower value being the most reasonable. Therefore, from this crude calculation it appears that the fracture energy dissipated by the matrix is comparable to the fracture energy absorbed by the fiber-matrix debonding process. However, to rationalize the apparent increase in energy absorption by the matrix with increase testing rate observed here a more precise equation may be needed.

#### Correlation of Debond Region Size With Interface Strength

In Figs. 11 and 12, mean plots of the unstressed fragment and debond lengths, respectively, are shown for E-glass/DGEBA/*m*-PDA test specimens where the degree of bonding at the fiber-matrix interface, and hence the interface strength, has been altered by coating one set of fibers with the NOTS coupling agent. All specimens were tested using the intermediate test protocol. In Fig. 11, the expected increase in the average fragment length with decrease bonding at the fiber-matrix interface is seen. The associated average debond lengths shown in Fig. 12 also reflect an increase in the corresponding length of the debond regions when the degree of bonding at the fiber-matrix interface is decreased. From these results the failure zone in a debond region correlates with changes in IFSS when the degree of bonding is altered at the fiber-matrix interface and the testing protocol remains constant.

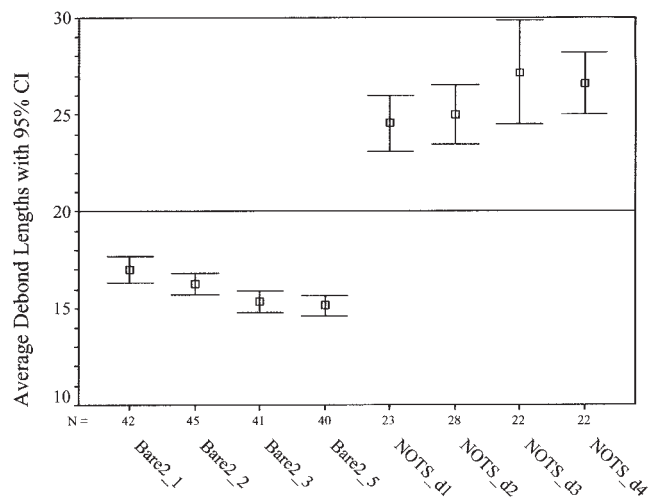


FIG. 12. Mean plot of unstressed debond lengths with 95% confidence intervals. All specimens were tested using the intermediate test protocol. The NOTS specimens are E-glass fibers coated with *n*-octadecyl triethoxysilane coupling agent.

## CONCLUSIONS

In this paper we have interpreted the occurrence of darker regions associated with fiber fracture in E-glass/DGEBA/*m*-PDA test specimens as regions of complete fiber-matrix debonding. From this interpretation of the experimental data, the matrix strain in the debond region at saturation ( $\approx 41.0\%$ ) is an order of magnitude higher than the global matrix strain ( $\approx 4.2\%$ ) at saturation. This result suggests that in the E-glass/DGEBA/*m*-PDA system matrix strain accounts for a significant amount of the increase in size of a debond region with increasing strain. Therefore, assessment of the fiber-matrix interface toughness using an energy balance approach may only be accurate when the energy dissipated through matrix strain is considered.

By measuring the size of a debond region in the unstressed state after testing and accounting for secondary debond growth after initial debond region formation, it was also shown that the initial size of a debond region at formation depends on the strain at formation and average size of the parent fragment (i.e., how close the system is to saturation). These results are consistent with the theoretical calculations of Nairn and Liu [17] which indicated that the initial debond length associated with a newly formed fiber break increases initially with increasing strain but reaches a maximum before saturation and decreases in size as saturation is reached. The experimental data also indicates a subtle but statistically significant change in the average size of the debond region formed during fiber fracture with testing protocol ( $\Delta = 1.3 \mu\text{m}$ ). Specifically, as the average testing rate increased, the average size of the debond region decreased, even though the average size of the fiber fragments increased. This result suggests that more of the strain energy released during fiber fracture is retained in the matrix as the testing rate is increased. It is not known at this time, if these data suggests an increased propensity of the matrix to form

matrix cracks at high strain rate, thereby increasing the rate at which critical flaws nucleate in composites. The result suggests, however, that a detailed investigation of the matrix modulus during the SFRT is warranted.

Finally, it was shown using a specific test protocol that the failure zone of a debond region increases as the IFSS decreases when the degree of bonding is changed at the fiber–matrix interface. In contrast, changes in testing rate resulted in an apparent decrease in the IFSS and a decrease in the average length of the debond regions. The factors controlling the latter observation are not clearly understood. It is believed, however, that the sensitivity of the debond region size to testing rate may depend on the IFSS, the nature of the chemical bonds promoting adhesion in the fiber–matrix interphase region, the viscoelastic properties of the matrix interphase region, and the viscoelastic properties of the bulk matrix.

## REFERENCES

1. G.A. Holmes, R.C. Peterson, D.L. Hunston, and W.G. McDonough, *Polym. Compos.*, **21**, 450 (2000).
2. R.K. Agrawal and L.T. Drzal, *J. Adhes.*, **29**, 63 (1989).
3. P. Feillard, G. Desarmot, and J.P. Favre, *Compos. Sci. Technol.*, **49**, 109 (1993).
4. J. Mullin, J.M. Berry, and A. Gatti, *J. Compos. Mater.*, **2**, 82 (1968).
5. A.T. DiBenedetto and P.J. Lex, *Polym. Eng. Sci.*, **29**, 543 (1989).
6. J.A. Nairn, 2000, Personal Communication on Fiber Matrix Debonding.
7. I. Hisayoshi and Y. Kagawa, *Philos. Mag. B*, **78**, 37 (1998).
8. N. Melanitis, C. Galiotis, P.L. Tetlow, and C.K.L. Davies, *J. Compos. Mater.*, **26**, 574 (1992).
9. I.M. Daniel and O. Ishai, *Engineering Mechanics of Composite Materials*, Oxford University Press (1994).
10. A.S. Carrara and F.J. McGarry, *J. Compos. Mater.*, **2**, 222 (1968).
11. H. Jahankhani and C. Galiotis, *J. Compos. Mater.*, **25**, 609 (1991).
12. A.N. Netravali, R.B. Hestenburg, S.L. Phoenix, and P. Schwartz, *Polym. Compos.*, **10**, 226 (1989).
13. L.T. Drzal and P.J. Herrera-Franco, "Composite Fiber-Matrix Bond Tests," in *Engineered Materials Handbook: Adhesives and Sealants*, ASM Int., Metals Park, Ohio, 391 (1990).
14. H.H. Ku, *J. Res. Natl. Bur. Stand. Sect. C*, **70**, 332, (1966).
15. H. Iba and Y. Kagawa, *Philos. Mag. B*, **78**, 37 (1998).
16. D.L. Hunston, R.J. Moulton, N.J. Johnston, and W.D. Bascom, "Matrix Resin Effects in Composite Delamination: Mode-I Fracture Aspects," in *Toughened Composites*, N.J. Johnston, ed., American Society for Testing and Materials, Philadelphia, 74 (1987).
17. J.A. Nairn and Y.C. Liu, *Compos. Struct.*, **4**, 241 (1997).
18. A. Kelly and W.R. Tyson, *J. Mech. Phys. Solids*, **13**, 329 (1965).